Synthesis and characterization of precursor derived TiN@Si–Al–C–N ceramic nanocomposites for oxygen reduction reaction

Eranezhuth Wasan Awin, Timon E. Günther, Rameshwori Loukrakpam, Stefan Schafföner, Christina Roth, Günter Motz

Angaben zur Veröffentlichung / Publication details:

Awin, Eranezhuth Wasan, Timon E. Günther, Rameshwori Loukrakpam, Stefan Schafföner, Christina Roth, and Günter Motz. 2023. "Synthesis and characterization of precursor derived TiN@Si–Al–C–N ceramic nanocomposites for oxygen reduction reaction." *International Journal of Applied Ceramic Technology* 20 (1): 59–69. https://doi.org/10.1111/ijac.14234.

Received: 16 May 2022 | Revised: 24 August 2022 | Accepted: 14 September 2022

DOI: 10.1111/ijac.14234

International Journal of Applied Ceramic Technology

SPECIAL ISSUE ARTICLE

Synthesis and characterization of precursor derived TiN@Si–Al–C–N ceramic nanocomposites for oxygen reduction reaction

Eranezhuth Wasan Awin[1] | **Timon E. Günther**[2] | **Rameshwori Loukrakpam**[2] | **Stefan Schafföner**[1] | **Christina Roth**[2] | **Günter Motz**[1]

[1]Department, of Ceramic Materials Engineering, University of Bayreuth, Bayreuth, Germany

[2]Department of Electrochemical Process Engineering, University of Bayreuth, Bayreuth, Germany

Correspondence
Günter Motz, Department of Ceramic Materials Engineering, University of Bayreuth, Prof.-Rüdiger Bormann-Str. 1, 95447 Bayreuth, Germany.
Email: guenter.motz@uni-bayreuth.de

Funding information
Deutsche Forschungsgemeinschaft; Agence Nationale de la Recherche

Editor's Choice
The Editor-in-Chief recommends this outstanding article.

Abstract

The development of efficient and durable catalysts is critical for the commercialization of fuel cells, as the catalysts' durability and reactivity dictate their ultimate lifetime and activity. In this work, amorphous silicon-based ceramics (Si–C–N and Si–Al–C–N) and TiN@Si–Al–C–N nanocomposites were developed using a precursor derived ceramics approach. In TiN@Si–Al–C–N nanocomposites, TiN nanocrystals (with sizes in the range of 5–12 nm) were effectively anchored on an amorphous Si–Al–C–N support. The nanocomposites were found to be mesoporous in nature and exhibited a surface area as high as 132 m^2/g. The average pore size of the nanocomposites was found to increase with an increase in the pyrolysis temperature, and a subsequent graphitization of free carbon was observed as revealed from the Raman spectra. The ceramics were investigated for electrocatalytic activity toward the oxygen reduction reaction using the rotating disk electrode method. The TiN@Si–Al–C–N nanocomposites showed an onset potential of 0.7 V versus reversible hydrogen electrode for oxygen reduction, which seems to indicate a 4-electron pathway at the pyrolysis temperature of 1000°C in contrast to a 2-electron pathway exhibited by the nanocomposites pyrolyzed at 750°C via the Koutecky–Levich plot.

KEYWORDS
catalysts/catalysis, characterization, nanocomposites, polymer precursor, silicon carbonitride

1 | INTRODUCTION

The global energy demand and environmental pollution drive the need for continuous improvement of existing sustainable energy devices. Out of which, electrocatalytic devices (e.g., fuel cells) have raised considerable interest due to their high energy density and power density.[1,2] The oxygen reduction reaction (ORR) is very important in electrocatalysis, and platinum-based electrocatalysts have been proven to be among the best in terms of their performance.[3] Currently, platinum on a carbon support is the most extensively used ORR catalyst. However, the use of noble metals increases the overall cost of the electrocatalytic devices. Furthermore, platinum-based electrocatalysts are also known to be not long-term stable under fuel cell working conditions.[4,5] Under these

circumstances, the need for alternative low-cost, robust, and stable electrocatalysts is substantial.

Owing to the high electrical conductivity, nitrogen-doped carbon materials and transition metal nitrides have been tested in previous projects and reported to exhibit promising ORR activity.[6–9] Herein, the presence of nitrogen is believed to raise the conduction band and thus increase the ORR activity.[10,11] There have been several studies using porous nitrogen–doped carbon materials as favorable electrocatalytic supports.[12–14] This includes nitrogen-doped carbon nanotubes/graphene,[15] carbon spheres,[16] carbon fibers,[17] and graphitic–C_3N_4.[18] Liu et al. reported an Si–C material in which bonding silicon to carbon was shown to excite electrons more readily to oxygen when compared to pristine graphene.[19] Furthermore, the electrochemical activity of transition metal nitrides on carbon supports was investigated, and high onset potentials and ORR current densities were observed.[20,21] Even though the aforementioned material systems exhibited significant ORR activity, the practical use of these materials is still restricted due to their poor corrosion resistance and scalability issues.[22,23]

In this context, silicon carbonitride (silicon-based precursor derived ceramics [PDC], Si–C–N), known for its excellent stability, chemical resistance, and ease in processability, could be a viable candidate for electrocatalysts. The presence of free carbon in the system could be a determining factor in enhancing the catalytic properties. The technical possibilities that PDCs have to offer, in particular, tailoring the ceramics properties at the molecular scale, make the approach appreciable for functional applications.[24–27] For instance, the addition of aluminum into the backbone of the Si–C–N network could enhance the electrical conductivity and is thereby believed to improve the electrocatalytic activity.[28] The functional properties could also be tuned by incorporating transition metal oxides, nitrides, and carbides into the structure. Hence, in this study, amorphous Si–C–N and silicon aluminum carbonitride (Si–Al–C–N) ceramics were synthesized using a PDC approach. In addition, a combinatorial technique that involves PDC with urea–glass route was used to produce TiN@Si–Al–C–N nanocomposites. The aforementioned materials were evaluated for their ORR activity.

2 | EXPERIMENTAL METHODS

2.1 | Synthesis of porous Si–C–N and Si–Al–C–N supports

In an attempt to synthesize porous Si–C–N, hydroxy-terminated polyethylene (PEOH) dissolved in toluene was made to react with polysilazane (Durazane 1800, Merck KGaA, Germany) in 70:30 by weight at 110°C under static conditions for 1 h to synthesize a block copolymer (HTT1800-b-PE). Because of its high crystallinity and reactive hydroxyl end group, the inexpensive PEOH was chosen as a latent pore former block and to connect with the HTT1800 block. To produce porous Si–Al–C–N ceramics, aluminum acetylacetonate (dissolved in toluene) was added to the aforementioned mixture in 90:10 weight ratio, and subsequently, cross-linking was commenced by the addition of dicumyl peroxide. The temperature of the preceramic polymeric mixture was maintained for 12 h and then cooled to room temperature. The solvent was then removed, and the resulting precursor was transferred to the tube furnace. The polymeric precursor was then pyrolyzed at 800°C in nitrogen atmosphere for half an hour to obtain porous Si–Al–C–N ceramics. During the heating cycle, heating rate was maintained at 1°C/min up to 300°C and then 5°C/min up to 800°C. Throughout the pyrolysis, the material was held at 300, 400, and 500°C for 2 h in nitrogen atmosphere.

2.2 | Synthesis of TiN nanocrystals anchored on porous Si–Al–C–N ceramic supports

TiN nanocrystals anchored on porous Si–Al–C–N ceramic supports were prepared using $TiCl_4$ (Merck KGaA, Germany) as a TiN precursor. In a typical synthesis procedure, 2.5 ml of ethanol was added to 1 g of $TiCl_4$ to which 1583 mg of urea (molar ratio of urea to $TiCl_4$ was maintained to be five) and 100 mg of Si–Al–C–N in 15 ml of ethanol were added subsequently. The mixture was stirred for 1 h, and the solution was kept at 100°C overnight to remove the solvent. The viscous mixture was then pyrolyzed at two different temperatures (750 and 1000°C) maintaining a heating rate of 3°C/min and held for 3 h in nitrogen atmosphere, which hereafter will be referred to as TiN@Si–Al–C–N_750 and TiN@Si–Al–C–N_1000.

2.3 | Materials characterization

The bonding characteristics were analyzed from Fourier transform infrared (FTIR) analysis (Bruker Tensor 27, USA). Raman spectroscopy was carried out using a Bruker SENTERRA II, USA confocal microscope with a 532 nm excitation laser to analyze the presence of free carbon. The crystalline nature of the prepared catalysts was evaluated by X-ray diffraction (XRD, D8 ADVANCE Bruker AXS, Germany). The micro/nanostructural characteristics were visualized using scanning electron microscopy (SEM,

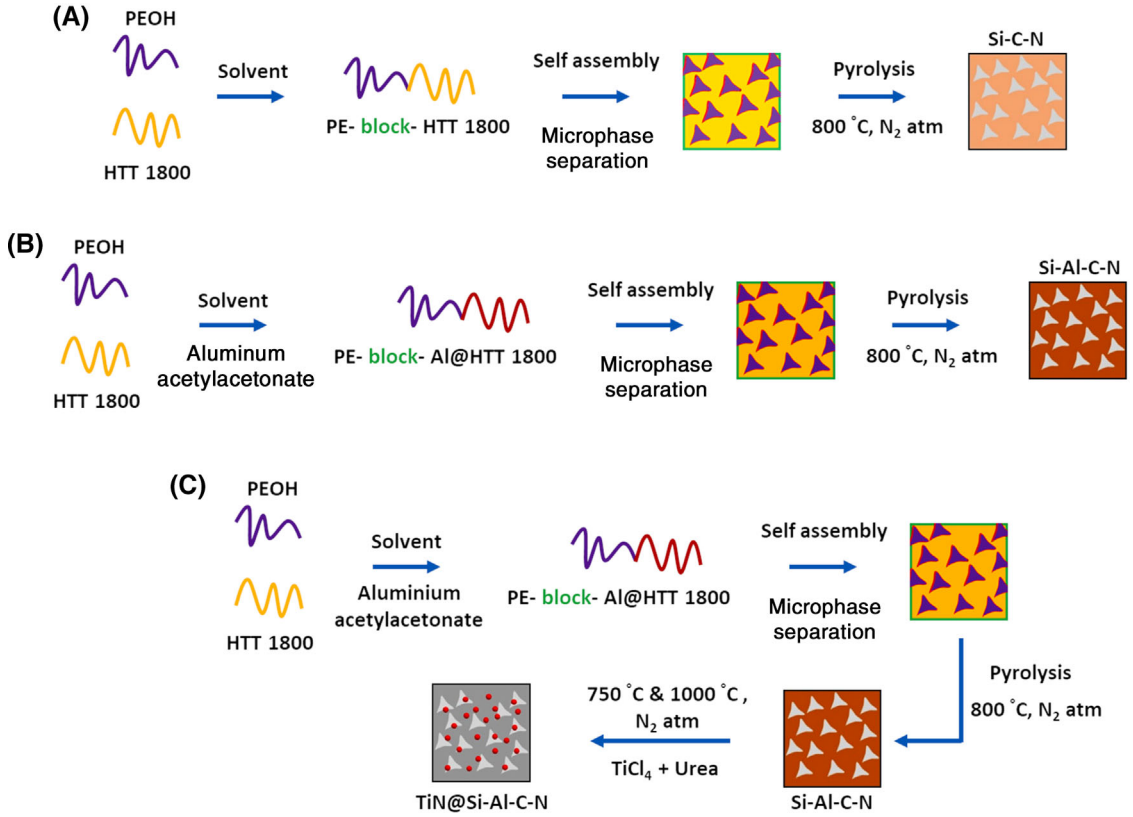

FIGURE 1 Generalized scheme for the synthesis of (A) Si–C–N ceramics, (B) Si–Al–C–N ceramics, and (C) TiN@Si–Al–C–N nanocomposites

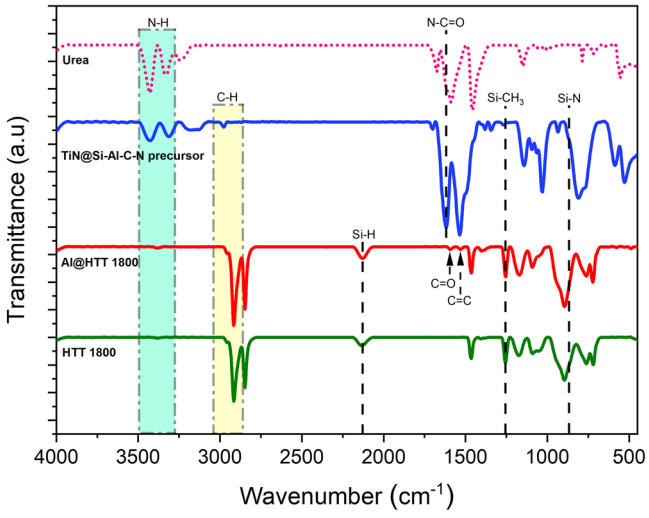

FIGURE 2 Fourier transform infrared (FTIR) spectra of HTT 1800, aluminum modified HTT 1800, and metal nitride precursors prepared using two different strategies

Gemini Sigma 300 VP, Carl Zeiss AG, Germany) and transmission electron microscopy (TEM) (JEOL JEM-2200FS, 200 kV, Germany). The porosity of the catalysts was determined using BET analysis (Nova 2000e, Quantachrome, USA).

2.4 | Electrochemical measurements

The evaluation of the ORR activity of the prepared silicon-based ceramics and the nanocomposites (hereafter referred to as catalysts) was performed using an electrochemical setup with Bio-Logic VSP 300 potentiostat and a Pine Research rotator controller. A standard electrochemical glass cell with a volume of 100 ml was used for the electrochemical performance tests. A three-electrode setup with a reversible hydrogen electrode (RHE, HydroFlex from Gaskatel) as reference electrode, platinum coil as counter electrode, and glassy carbon electrode RDE tip ($\varnothing = 5$ mm) with a catalyst layer as the working electrode was employed in .1 M KOH electrolyte and kept at 25°C. The glassy carbon RDE tip was first polished with alumina particles of (average) size .3 and .05 μm in suspension (from Buehler) and rinsed with ultrapure water (Milli-Q, 18.2 MΩ cm). The preparation of the catalyst layer is as follows: 10 mg of the catalyst powder was taken, and 2.5 ml ultrapure water and 2.5 ml isopropanol were added, then 50 μl of 10 wt% Nafion solution (from Alfa Aesar) was added to it. The glass vial containing the mixture was placed in an ultrasonic bath filled with cold water (<5°C) and sonicated (37 kHz, 100% Power, Elmasonic P) for 15 min. For preparing the catalyst film, a volume of

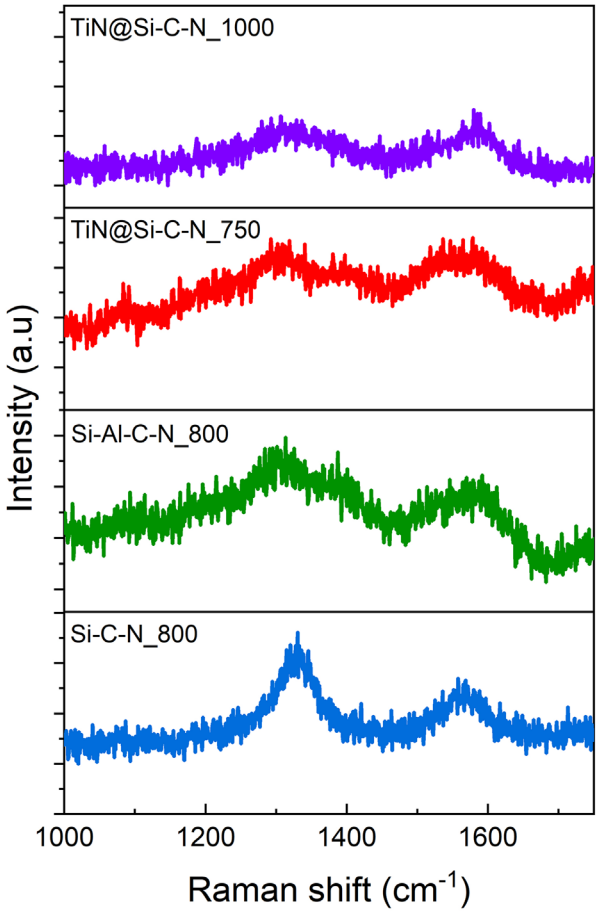

FIGURE 3 Raman spectra of synthesized silicon-based ceramics indicating the presence of free carbon by the characteristic D and G band

TABLE 1 Variation of I_D/I_G ratio of Si–C–N ceramics with the modification of Al and TiN

Samples	I_D/I_G
Si–C–N	1.91
Si–Al–C–N	1.60
TiN@Si–Al–C–N_750	1.13
TiN@Si–Al–C–N_1000	.93

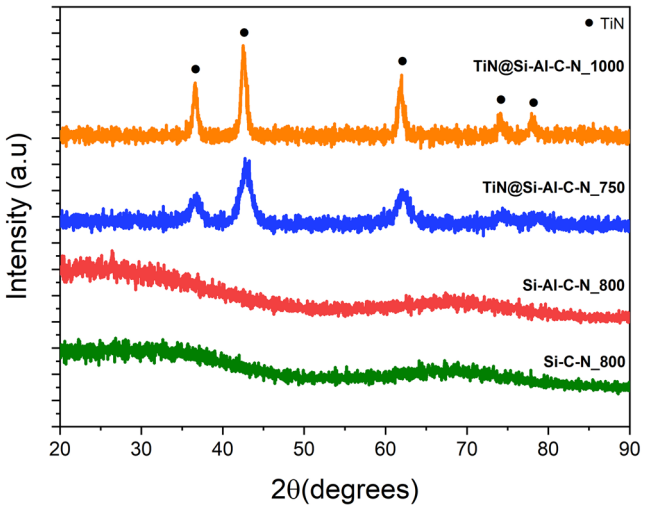

FIGURE 4 X-ray diffractograms of synthesized silicon-based ceramics revealing the amorphous nature of the substrates and crystallization of titanium nitride after pyrolysis

50 μl was dropped in several steps on the cleaned and polished glassy carbon electrode (geometrical surface area .196 cm^2) that was dried during rotation at 700 rpm under ambient conditions. Pretreatment steps in electrolyte saturated with N_2 and O_2 were done on the RDE tips with a catalyst layer using cyclic voltammograms (CVs) in a potential range of +.1 to +1.0 V versus RHE with a scan rate of 200 mV/s (50 cycles each) to activate the surface of the catalysts. Open circuit voltage (OCV) was held for 30 min with gas bubbling before recording the CVs. The ohmic drop was compensated at 85% using a positive feedback method, which left an uncompensated resistance of ~5 Ω or less in the electrochemical cell. RDE measurements were carried out at the rotating speeds of 100, 400, 900, 1600, and 2200 rpm using linear sweep voltammetry (LSV) to record the current densities (mA/cm^2 of the geometrical surface area) in saturated O_2 in the potential range of .05–1.2 V with 20 mV/s scan rate. Three cycles were recorded for each rotating speed, and the third cycle was used for analysis. Additionally, the N_2 background current was collected for the same potential range and scan rate at 1600 rpm and subtracted from the ORR current densities to eliminate any capacitive current. Reported results are based on kinetic parameters of the Koutecky–Levich equations. An additional CV was performed with 5 mV/s scan rate in O_2 saturated electrolyte with no rotation. OCV was held for 15 min to saturate the electrolyte with O_2 before chrono-amperometric (CA) measurements on TiN@Si–Al–C–N_1000 at the potential of .6 V for 2 h. The ORR activity was recorded for TiN@Si–Al–C–N_1000, in O_2-saturated .1 M KOH solution with a slow scan rate of 5 mV/s and a rotation rate of 1600 rpm before and after the CA.

3 | RESULTS AND DISCUSSION

Figure 1 represents the generalized scheme of reactions used to synthesize Si–C–N, Si–Al–C–N and TiN@Si–Al–C–N ceramics. The first stage involves the synthesis of Si–C–N ceramics by reacting HTT 1800 with PEOH. This led to the formation of PE-block-HTT1800 by self-assembly that upon pyrolysis in nitrogen atmosphere decomposes to form amorphous and porous Si–C–N. In order to synthesize aluminum modified Si–C–N ceramics, aluminum

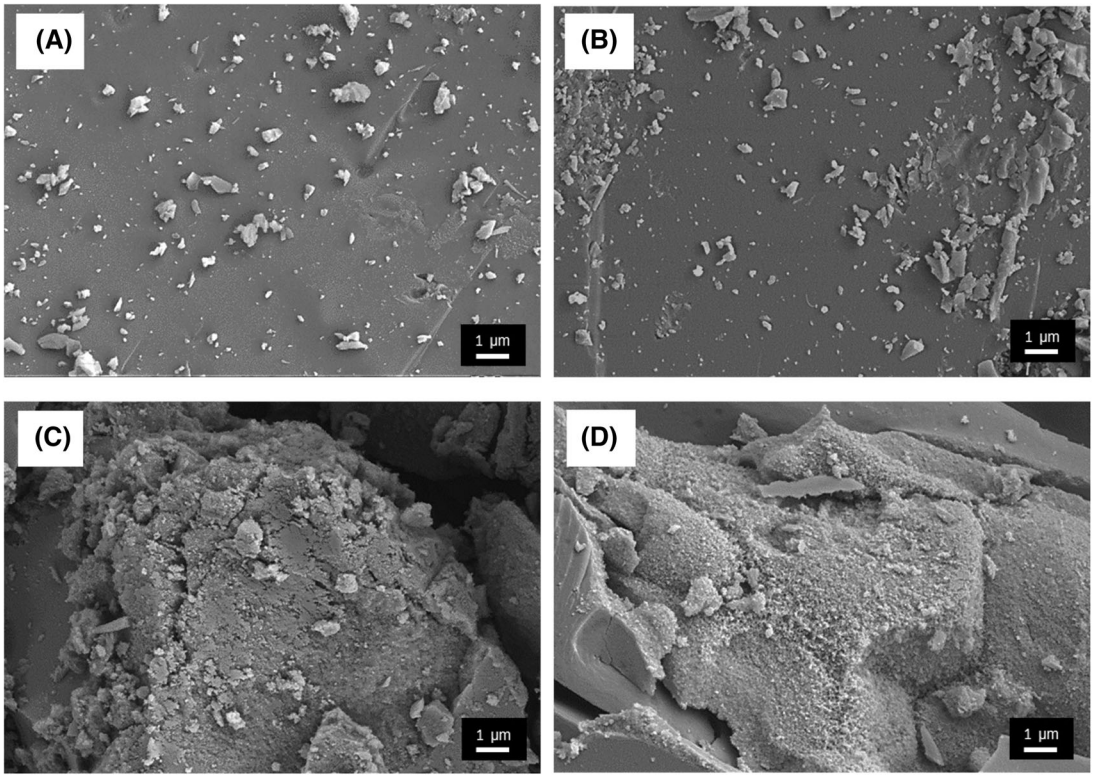

FIGURE 5 Scanning electron micrographs of (A) Si–C–N, (B) Si–Al–C–N, (C) TiN@Si–Al–C–N_750, and (D) TiN@Si–Al–C–N_1000 nanocomposites indicating the evolution of porosity with respect to pyrolysis temperature

acetylacetonate was added to the aforementioned reaction mixture and pyrolyzed in nitrogen atmosphere.

In order to understand the bonding characteristics, the FTIR spectra of the starting precursors were taken and plotted in Figure 2 and compared. There was no noticeable difference in peaks between HTT1800 and Al modified HTT1800. However, the peaks at 1592 cm^{-1} (C=O stretching) and 1531 cm^{-1} (C=C stretching) could be assigned to the characteristic bands of aluminum acetylacetonate.[29,30] The peaks observed at 3385 cm^{-1} (N–H stretching), 2917 cm^{-1} (C–H stretching), 2125 cm^{-1} (Si–H stretching), 1260 cm^{-1} (C–H symmetric deformation), and 891 cm^{-1} (Si–N stretching) correspond to polysilazane. In the case of TiN@Si–Al–C–N precursor, the peaks observed at 3385 cm^{-1} (N–H asymmetric vibrations) and 3320 cm^{-1} (N–H symmetric vibrations) could be assigned to urea. The peak at 1620 cm^{-1} could be assigned to the presence of N–C=O bonds. The absence of Si–H peaks in the TiN@Si–Al–C–N precursor implies the complete ceramization of the Si–Al–C–N substrate at the chosen pyrolysis temperature (800°C).

Raman spectroscopy was performed to analyze the presence of free carbon in the prepared ceramics. The Raman spectra clearly revealed the presence of free carbon for Si–C–N, Si–Al–C–N, TiN@Si–Al–C–N_750, and TiN@Si–Al–C–N_1000 nanocomposites as shown in Figure 3 by clear D:G peaks characteristic of carbonaceous species.

The bands at ~1320 and ~1580 cm^{-1} correspond to disordered carbon and in-plane vibrations of graphitic sp^2 carbon, respectively. The I_D/I_G ratio (Table 1) was found to be decreasing with the modification of Si–C–N by Al and TiN (from 1.91 to .93). In the case of TiN@Si–Al–C–N_750 and TiN@Si–Al–C–N_1000 nanocomposites, the decrease in I_D/I_G ratio with increase in pyrolysis temperature indicates progressive graphitization.[31,32] This is expected to increase the electrical conductivity of the nanocomposites, thereby improving the electrocatalytic activity.[33]

The XRD patterns of the synthesized materials are shown in Figure 4. The Si–C–N and Si–Al–C–N ceramics were found to be amorphous in nature indicated by their featureless diffractograms. The TiN@Si–Al–C–N nanocomposites exhibited broad peaks at 2θ = 36.6°, 42.8°, 62.2°, and 74.4° indicating the nanocrystalline nature of crystalline TiN. The size of the nanocrystalline TiN pyrolyzed at 750 and 1000°C was determined using Scherrer's formula and estimated to be 5 and 12 nm, respectively.

Figure 5 shows the SEM micrographs of the prepared catalysts. The addition of Al in the Si–C–N backbone (Figure 5B) did not cause visible changes to the microstructure of the powders. However, the introduction of TiN

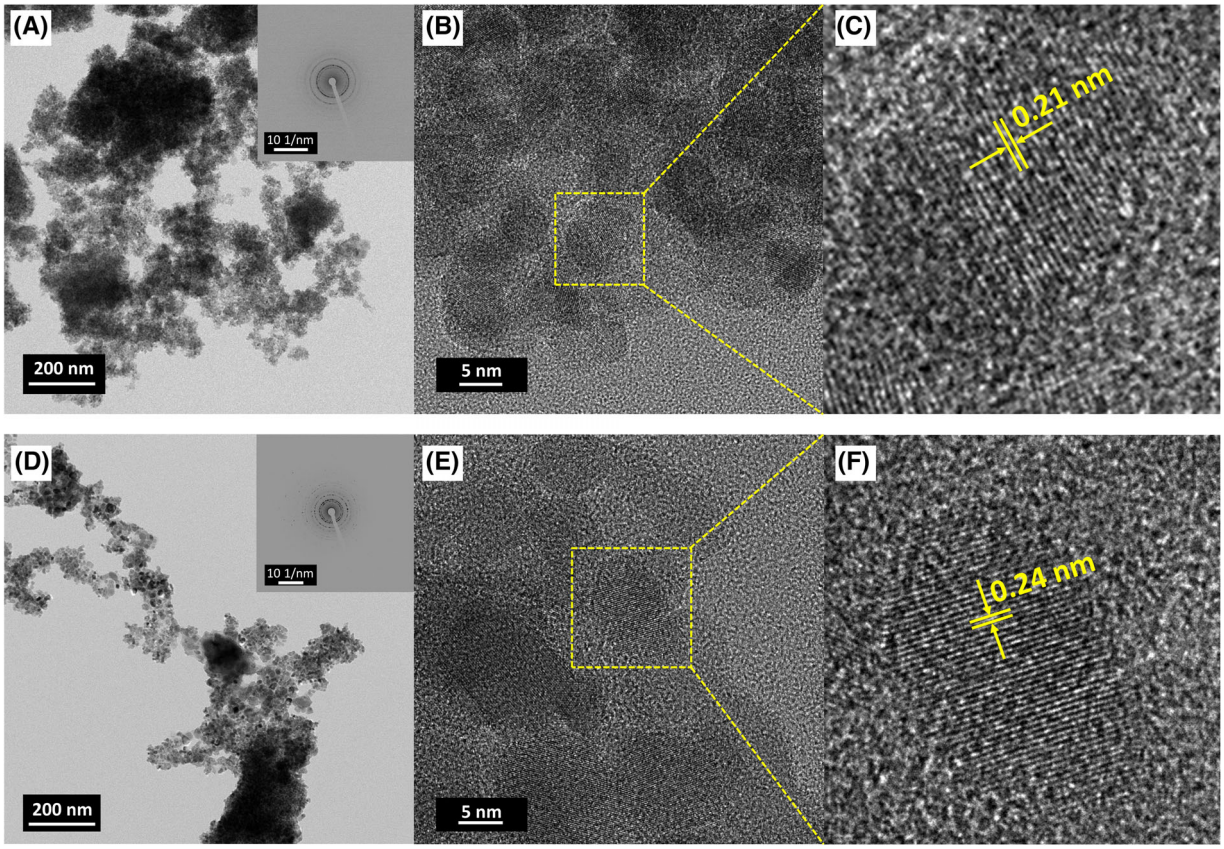

FIGURE 6 High resolution transmission electron microscopy (HRTEM) images of (A–C) TiN@Si–Al–C–N_750 and (D–F) TiN@Si–Al–C–N_1000 nanocomposites indicating the uniformly distributed TiN nanocrystals in the Si–Al–C–N matrix. The inset image corresponds to the SAED patterns for the synthesized nanocomposites.

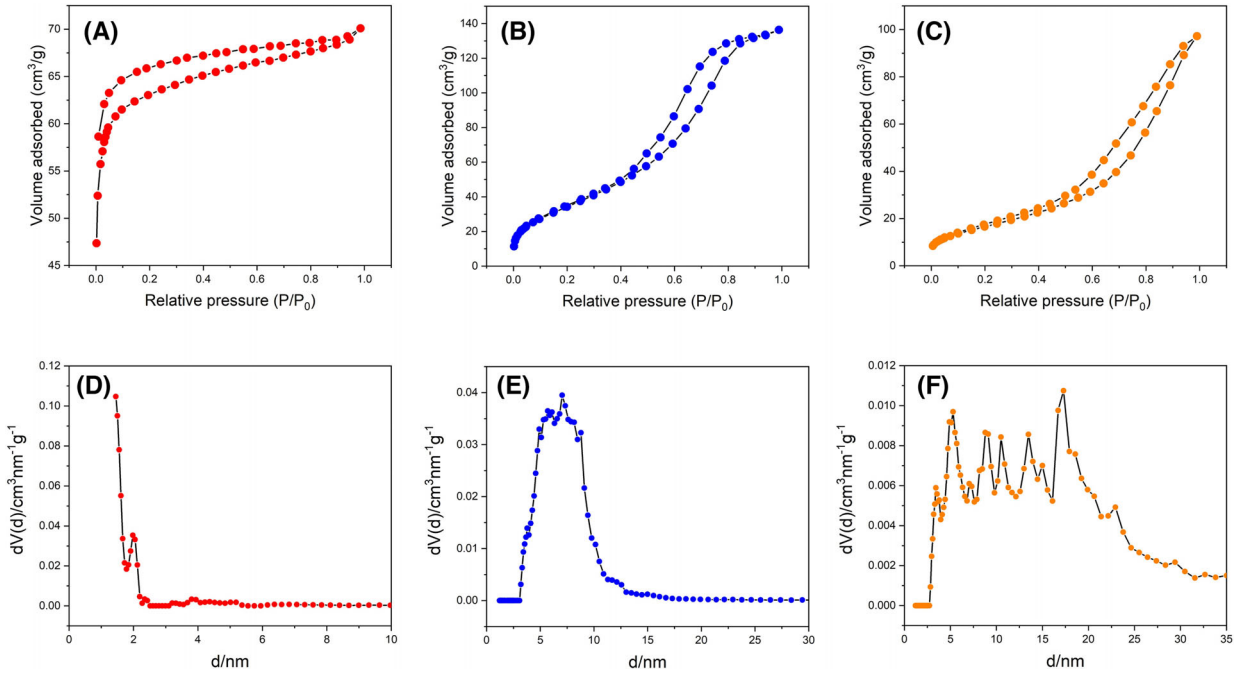

FIGURE 7 Nitrogen adsorption–desorption isotherms and pore size distribution of (A and D) Si–Al–C–N, (B and E) TiN@Si–Al–C–N_750, and (C and F) TiN@Si–Al–C–N_1000 revealing the porous nature of the prepared ceramics

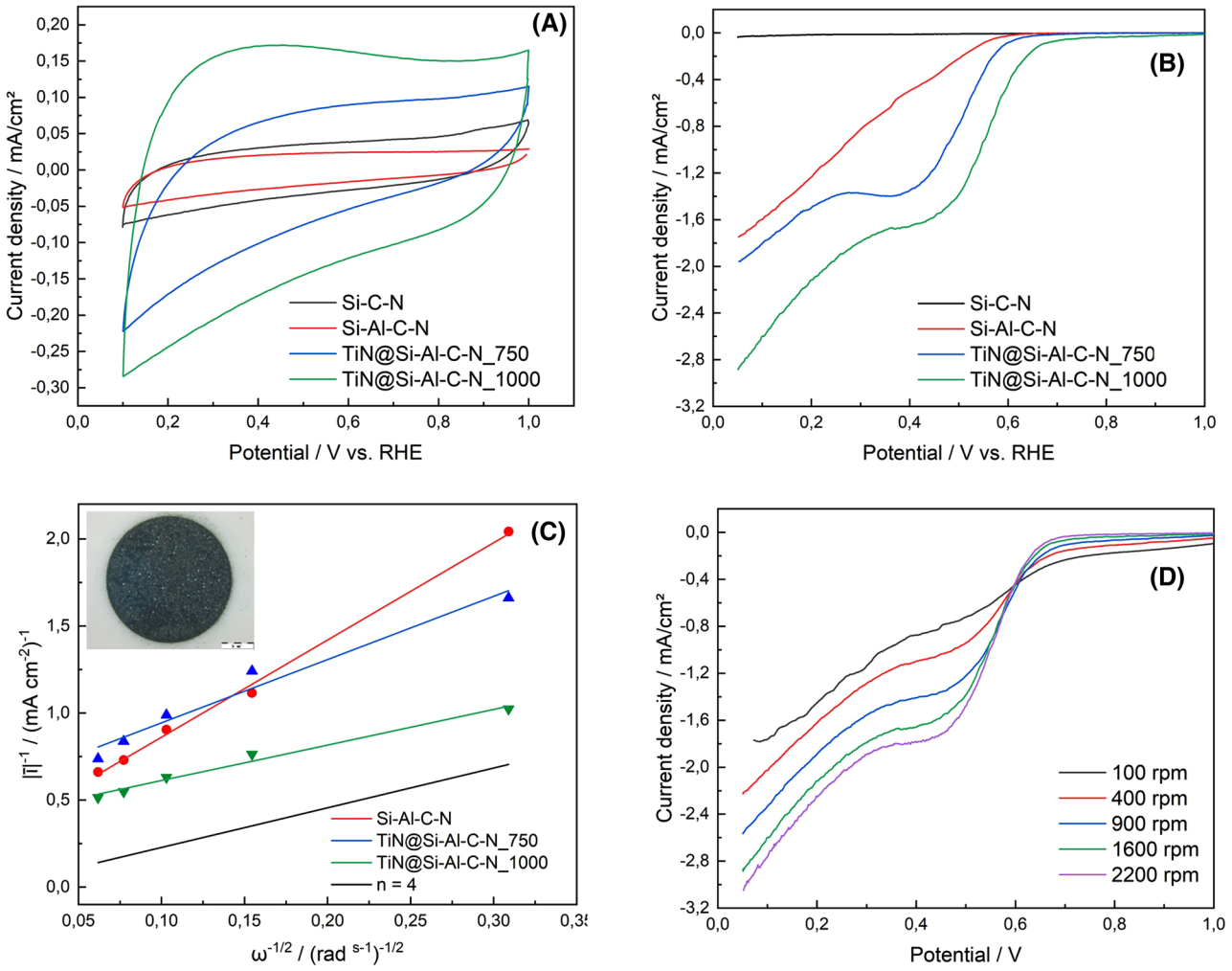

FIGURE 8 (A) Cyclic voltammogram (CV) curves of Si–C–N, Si–Al–C–N, TiN@Si–Al–C–N_750, and TiN@Si–Al–C–N_1000 in N_2-saturated .1 M KOH at a sweep rate of 200 mV/s (B) RDE voltammograms of Si–C–N, Si–Al–C–N, TiN@Si–Al–C–N_750, and TiN@Si–Al–C–N_1000 in O_2-saturated .1 M KOH at 1600 rpm at a scan rate of 20 mV/s, (C) Koutecky–Levich plots of the catalyst materials at 100, 400, 900, 1600, and 2200 rpm in reference to $n = 4$ of the exchanged number of electrons, (D) linear sweep voltammetry (LSV) scans of the TiN@Si–Al–C–N_1000 in O_2-saturated .1 M KOH at 100, 400, 900, 1600, and 2200 rpm with a scan rate of 20 mV/s

led to a change in the microstructures as shown in Figure 5C,D revealing the porous nature of the nanocomposites. The TiN@Si–Al–C–N nanocomposites exhibited TiN nanocrystals anchored on the Si–Al–C–N matrix. Moreover, the micrographs of TiN@Si–Al–C–N nanocomposites pyrolyzed at different temperatures clearly demonstrated the porous nature of the nanocomposites.

High-resolution transmission electron microscopy (HRTEM) was performed to visualize the distribution of TiN nanocrystals in the Si–Al–C–N matrix. Figure 6 shows HRTEM images of (A–C) TiN@Si–Al–C–N_750 and (D–F) TiN@Si–Al–C–N_1000 nanocomposites. The micrographs clearly revealed the uniform distribution of TiN nanocrystals in the Si–Al–C–N matrix. The measured crystallite size of TiN nanocrystals was in accordance with the crystallite size determined using Scherrer's formula. Figure 6C,F shows the lattice fringe spacing of TiN@Si–Al–C–N_750 and TiN@Si–Al–C–N_1000 nanocomposites, respectively. The lattice fringe spacing of .21 and .24 nm corresponds to the (200) and (111) planes of TiN, respectively. The inset images in Figure 6A,D correspond to SAED patterns of TiN@Si–Al–C–N_750 and TiN@Si–Al–C–N_1000 nanocomposites, respectively. The discontinuous ring patterns observed in SAED further confirm the crystalline nature of the nanocomposites.

The nitrogen-desorption measurements were performed on the prepared catalysts to understand their textural characteristics and revealed surface areas as shown in Figure 7. The surface areas of Si–Al–C–N, TiN@Si–Al–C–N_750, and TiN@Si–Al–C–N_1000 nanocomposites were found to be 191, 132, and 58 m^2/g, respectively. The Si–Al–C–N ceramics and TiN@Si–Al–C–N nanocomposites exhibited type IV isotherms with H2 hysteresis loop indicating the mesoporous nature (pore

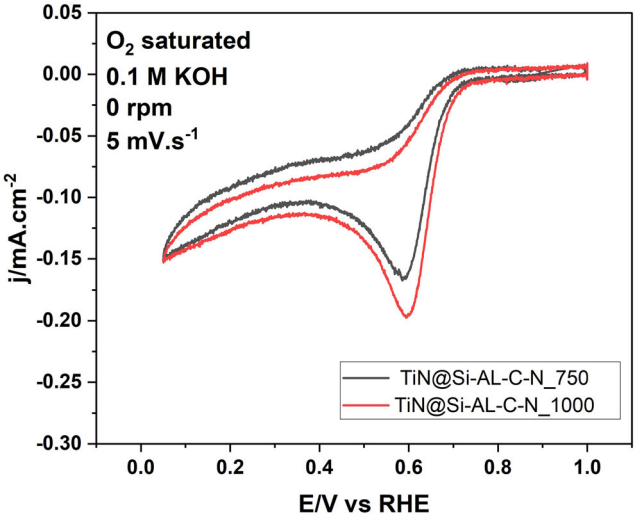

FIGURE 9 Cyclic voltammograms (CVs) of TiN@Si–Al–C–N_750 and TiN@Si–Al–C–N_1000, performed in O_2-saturated .1 M KOH solution with a slow scan rate of 5 mV/s (no rotation)

size in the range of 2–50 nm) of the nanocomposites. Furthermore, rather the high adsorption of nitrogen molecules at lower relative pressures $P/P_0 < .1$ indicates the presence of micropores. It was observed that the crystallization of TiN nanocrystals on Si–Al–C–N substrate decreased the amount of adsorbed nitrogen. The average pore size was determined by DFT calculations (N_2 at −196.15°C on carbon [slit pore model, NLDFT equilibrium model]), and the corresponding NLDFT pore size distributions have been shown in Figure 7D–F. The average pore sizes of Si–Al–C–N, TiN@Si–Al–C–N_750, and TiN@Si–Al–C–N_1000 were found to be 1.5, 7, and 17.2 nm, respectively. The average pore size of the nanocomposites was found to increase with an increase in the pyrolysis temperature.

The ORR performance of the synthesized Si–C–N, Si–Al–CN, TiN@Si–Al–C–N_750, and TiN@Si–Al–C–N_1000 has been thoroughly investigated and reported in Figure 8.

The CV curves in N_2-saturated .1 M KOH solution are shown in Figure 8A. No specific redox peaks were observed in a potential range from .1 to 1.0 V. The curves only show non-Faradaic currents with charge and discharge of the electric double layers. Si–C–N and Si–Al–C–N supports show low double layer capacitance, whereas the non-Faradaic current of the TiN-based catalysts increases with the pyrolysis temperature. This might be caused by the amount of carbon in the support material, which depends on the pyrolysis temperature and also affects the electrical conductivity. Figure 8B shows the ORR activity measured by the LSV polarization curve of the Si–Al–C–N and TiN@Si–Al–C–N (pyrolyzed at 750 and 1000°C) catalysts at a sweep rate of 20 mV/s and a rotation speed of 1600 rpm. It can be seen that the different samples exhibit significantly different current densities. Although the Si–C–N support does not contribute to ORR, the activity increases to about 1.7 mA/cm^2 when Al is added into the sample. Higher ORR activities are measured for the pyrolyzed TiN samples. The carbon content varies with pyrolysis temperature and therefore has a significant effect on the limiting current density and onset potential. The current densities for Si–C–N, Si–Al–C–N, TiN@Si–Al–C–N_750, and TiN@Si–Al–C–N_1000 at .58 V are .006, .04, .15, and .6 mA/cm^2, respectively. The corresponding plots for the Koutecky–Levich (*K–L*) analysis are shown in Figure 8C. *K–L* plots allow us to evaluate the first-order reaction, knowing the amount of dissolved oxygen in the electrolyte and the calculation of the electron transfer number per oxygen molecule during ORR. Figure 8D shows the LSV curves for TiN@Si–Al–C–N_1000 at various rotating speeds. The number of transferred electrons for Si–C–N, Si–Al–C–N, TiN@Si–Al–C–N_750, and TiN@Si–Al–C–N_1000 in a potential range from .35 to .55 V was calculated as .008, 1.63, 2.23, and 3.85 electrons, in comparison to the desired 4e$^-$ process, which is obtained during the catalysis of ORR by the noble metal Pt.

The CVs of TiN@Si–Al–C–N_750 and TiN@Si–Al–C–N_1000 were also performed at a slow scan rate of 5 mV/s in O_2-saturated .1 M KOH solution with no rotation. A similar correlation between TiN@Si–Al–C–N_750 and TiN@Si–Al–C–N_1000 was observed as shown in Figure 9.

The reported onset potential of TiN-based catalysts was between .5 and .83 V. For instance, .6 V has been reported for bulk TiN,[20] .85 V for TiN hollow spheres,[34] .83 V for TiN/graphene-CNT,[20] and .5 V for TiON@nitrogen-doped carbon spheres.[9] In this study, the onset potential of TiN@Si–Al–C–N_1000 was found to be .7 V.

In order to understand the stability of the catalyst, CA was performed on TiN@Si–Al–C–N_1000 at the potential of .6 V for 2 h (Figure 10A), where we observed significant activity in the ORR curve. After a hold time at OCV for 15 min, the current stabilized at around −.02 mA and was stable for the whole duration of the CA. The CVs (anodic scans) of TiN@Si–Al–C–N_1000, in O_2-saturated .1 M KOH solution with a slow scan rate of 5 mV/s and a rotation rate of 1600 rpm, are reported in Figure 10B before and after the stability test. It can be seen that a slight increase in the catalytic activity was observed after the CA treatment.

SEM images of the TiN@Si–Al–C–N_1000 nanocomposites were obtained after the ORR test, and an exemplary micrograph is shown in Figure 11. There was no significant change observed in the microstructure (apart from a slight decrease in the porosity) post ORR test implying the stability during the test time frame of the prepared nanocomposites. However, it needs to be considered that the testing time was comparatively low. Furthermore, as

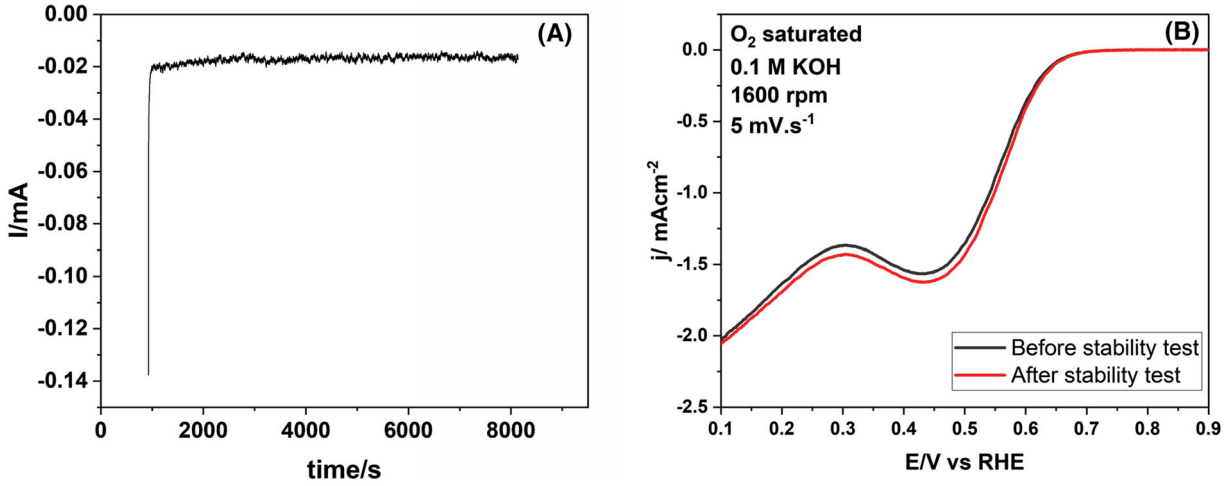

FIGURE 10 **(A)** Stability test (chrono-amperometric [CA]) of TiN@Si–Al–C–N_1000 performed in O_2-saturated .1 M KOH at .6 V for 2 h. **(B)** cyclic voltammograms (CVs) (anodic scan) of TiN@Si–Al–C–N_1000, performed in O_2-saturated .1 M KOH solution with a slow scan rate of 5 mV/s (1600 rotation)

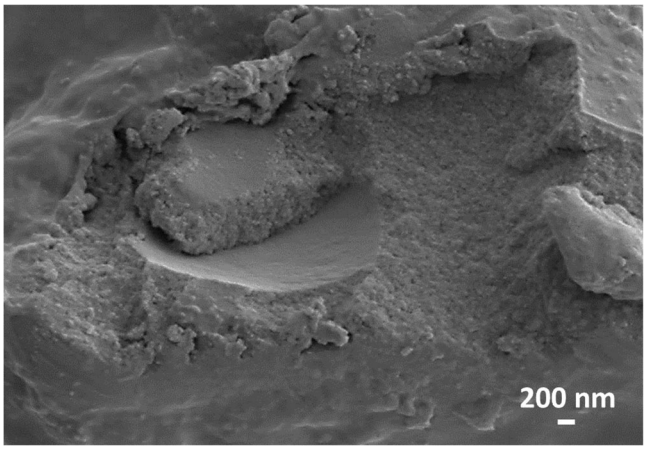

FIGURE 11 Scanning electron micrograph of TiN@Si–Al–C–N_1000 nanocomposites after oxygen reduction reaction (ORR) test

the catalyst film on the RDE is very thin, not enough post material could be collected for further testing by BET, Raman, and XRD.

4 | CONCLUSIONS

TiN@Si–Al–C–N nanocomposites were prepared using a combination of PDC approach with urea–glass route. The synthesized nanocomposites were explored for their electrocatalytic (ORR) properties in alkaline media using RDE. The XRD diffractograms revealed the crystallization of TiN in an amorphous Si–Al–C–N matrix with sizes ranging from 5 to 12 nm. The SEM micrographs also confirmed the anchoring of TiN nanocrystals on an Si–Al–C–N substrate. The prepared TiN@Si–Al–C–N nanocomposites possessed a surface area of 132 and 58 m^2/g at 750 and 1000°C, respectively, and were found to be mesoporous in nature. The presence of TiN on the silicon-based ceramics was found to trigger an ORR response in alkaline media. Si–C–N, Si–Al–C–N, and TiN@Si–Al–C–N_750 led to a two-electron pathway with H_2O_2 formation in ORR, whereas TiN@Si–Al–C–N_1000 led to a four-electron pathway for the ORR in alkaline media. In the future, other electrocatalytically active centers, such as Fe that is also low-cost, non-toxic, and earth-abundant, could be implemented into these promising N-containing support materials, further increasing activity without the compromising stability of the materials.

ACKNOWLEDGMENTS

The authors would like to thank the Deutsche Forschungsgemeinschaft (DFG) and the Agence Nationale de la Recherche (ANR) for funding the work through the RECIFE project (Project Numbers: DFG MO851/22-1 and ANR-21-CE08-0036-01).

Open access funding enabled and organized by Projekt DEAL.

ORCID

Timon E. Günther https://orcid.org/0000-0002-3678-0999
Stefan Schafföner https://orcid.org/0000-0002-6526-2496
Günter Motz https://orcid.org/0000-0002-8010-068X

REFERENCES

1. Shimizu K, Sepunaru L, Compton RG. Innovative catalyst design for the oxygen reduction reaction for fuel cells. Chem Sci. 2016;7(5):3364–9.

2. Lori O, Elbaz L. Advances in ceramic supports for polymer electrolyte fuel cells. Catalysts. 2015;5(3):1445–64.
3. Shao M, Chang Q, Dodelet JP, Chenitz R. Recent Advances in electrocatalysts for oxygen reduction reaction. Chem Rev. 2016;116:3594–657.
4. Chung HT, Cullen DA, Higgins D, Sneed BT, Holby EF, More KL, et al. Direct atomic-level insight into the active sites of a high-performance PGM-free ORR catalyst. Science. 2017;357(6350):479–84. Available from: https://www.science.org
5. Guo D, Shibuya R, Akiba C, Saji S, Kondo T, Nakamura J. Active sites of nitrogen-doped carbon materials for oxygen reduction reaction clarified using model catalysts. Science. 2016;351(6271):361–5. Available from: https://www.science.org
6. Dong Y, Wu Y, Liu M, Li J. Electrocatalysis on shape-controlled titanium nitride nanocrystals for the oxygen reduction reaction. ChemSusChem. 2013;6(10):2016–21.
7. Yuan Y, Wang J, Adimi S, Shen H, Thomas T, Ma R, et al. Zirconium nitride catalysts surpass platinum for oxygen reduction. Nat Mater. 2020;19:280–6.
8. Zheng S, Luo R, Meng Z, Wang R, Tan H, Xia Y, et al. Recent advances in the electrocatalytic application of transition metal nitrides nanocrystalline. Preprints. 2021;2021040504:1–22.
9. Wassner M, Eckardt M, Reyer A, Diemant T, Elsaesser MS, Behm RJ, et al. Synthesis of amorphous and graphitized porous nitrogen- doped carbon spheres as oxygen reduction reaction catalysts. Beilstein J Nanotechnol. 2020;11:1–15.
10. Wang H, Keum JK, Hiltner A, Baer E, Freeman B, Rozanski A, et al. Confined crystallization of polyethylene oxide in nanolayer assemblies. Science (80–). 2009;323(5915):757–60.
11. Zhang L, Xia Z. Mechanisms of oxygen reduction reaction on nitrogen-doped graphene for fuel cells. J Phys Chem C. 2011;115(22):11170–6.
12. Lv Q, Si W, He J, Sun L, Zhang C, Wang N, et al. Selectively nitrogen-doped carbon materials as superior metal-free catalysts for oxygen reduction. Nat Commun. 2018;9(1):1–11.
13. Su F, Tian Z, Poh CK, Wang Z, Lim SH, Liu Z, et al. Pt nanoparticles supported on nitrogen-doped porous carbon nanospheres as an electrocatalyst for fuel cells. Chem Mater. 2010;22(3):832–9.
14. Li M, Xu F, Li H, Wang Y. Nitrogen-doped porous carbon materials: promising catalysts or catalyst supports for heterogeneous hydrogenation and oxidation. Catal Sci Technol. 2016;6:3670–93.
15. Zheng Y, He F, Wu J, Ma D, Fan H, Zhu S, et al. Nitrogen-doped carbon nanotube-graphene frameworks with encapsulated Fe/Fe_3N nanoparticles as catalysts for oxygen reduction. ACS Appl Nano Mater. 2019;2(6):3538–47.
16. Shi Q, Zhu C, Engelhard MH, Du D, Lin Y. Highly uniform distribution of Pt nanoparticles on N-doped hollow carbon spheres with enhanced durability for oxygen reduction reaction. RSC Adv. 2017;7(11):6303–8.
17. Bokach D, ten Hoopen S, Muthuswamy N, Buan MEM, Rønning M. Nitrogen-doped carbon nanofiber catalyst for ORR in PEM fuel cell stack: performance, durability and market application aspects. Int J Hydrogen Energy. 2016;41(39):17616–30.
18. Sarkar S, Kamboj N, Das M, Purkait T, Biswas A, Dey RS. Universal approach for electronically tuned transition-metal-doped graphitic carbon nitride as a conductive electrode material for highly efficient oxygen reduction reaction. Inorg Chem. 2020;59(2):1332–9.
19. Liu Z, Fu X, Li M, Wang F, Wang Q, Kang G, et al. Novel silicon-doped, silicon and nitrogen-codoped carbon nanomaterials with high activity for the oxygen reduction reaction in alkaline medium. J Mater Chem A. 2015;3(7):3289–93.
20. Youn DH, Bae G, Han S, Kim JY, Jang JW, Park H, et al. A highly efficient transition metal nitride-based electrocatalyst for oxygen reduction reaction: TiN on a CNT-graphene hybrid support. J Mater Chem A. 2013;1(27):8007–15.
21. Zeng R, Yang Y, Feng X, Li H, Gibbs LM, Disalvo FJ, et al. Non-precious transition metal nitrides as efficient oxygen reduction electrocatalysts for alkaline fuel cells. Sci Adv. 2022;8:eabj1584. Available from: https://www.science.org
22. Borup R, Meyers J, Pivovar B, Kim YS, Mukundan R, Garland N, et al. Scientific aspects of polymer electrolyte fuel cell durability and degradation. Chem Rev. 2007;107:3904–51.
23. McCreery RL. Advanced carbon electrode materials for molecular electrochemistry. Chem Rev. 2008;108:2646–87.
24. Colombo P, Mera G, Riedel R, Sorarù GD. Polymer-derived ceramics: 40 years of research and innovation in advanced ceramics. J Am Ceram Soc. 2010;93(7):1805–37. Available from: http://doi.wiley.com/10.1111/j.1551-2916.2010.03876.x
25. Mera G, Gallei M, Bernard S, Ionescu E. Ceramic nanocomposites from tailor-made preceramic polymers. Nanomaterials. 2015;5:468–540.
26. Awin EW, Lale A, Nair Hari Kumar KC, Demirci UB, Bernard S, Kumar R. Novel precursor-derived meso-/macroporous TiO2/SiOC nanocomposites with highly stable anatase nanophase providing visible light photocatalytic activity and superior adsorption of organic dyes. Materials (Basel). 2018;11(3):362.
27. Viard A, Kurz H, Lale A, Heymann L, Weber B, Bernard S, et al. Superparamagnetic silicon carbonitride ceramic fibers through in situ generation of iron silicide nanoparticles during pyrolysis of an iron-modified polysilazane. ACS Appl Mater Interfaces. 2021;13(7):8745–53.
28. David L, Asok D, Singh G. Synthesis and extreme rate capability of Si-Al-C-N functionalized carbon nanotube spray-on coatings as li-ion battery electrode. ACS Appl Mater Interfaces. 2014;6(18):16056–64.
29. Sorarù GD, Mercadini M, Maschio RD, Taulelle F, Babonneau F. Si-Al-O-N fibers from polymeric precursor: synthesis, structural and mechanical characterization. J Am Ceram Soc. 1993;76(10):2595–600.
30. Yang L, Zhang P, Feng Y, Yu Z. Single-source-precursor synthesis and characterization of SiAlC(O) ceramics from a hyperbranched polyaluminocarbosilane. High Temp Mater Processes. 2022;41:150–60.
31. Mera G, Riedel R, Poli F, Müller K. Carbon-rich SiCN ceramics derived from phenyl-containing poly(silylcarbodiimides). J Eur Ceram Soc. 2009;29(13):2873–83.
32. Gao Y, Mera G, Nguyen H, Morita K, Kleebe HJ, Riedel R. Processing route dramatically influencing the nanostructure of carbon-rich SiCN and SiBCN polymer-derived ceramics. Part I: Low temperature thermal transformation. J Eur Ceram Soc. 2012;32(9):1857–66.

33. Feng Y, Yu Z, Riedel R. Enhanced hydrogen evolution reaction catalyzed by carbon-rich Mo4.8Si3C0.6/C/SiC nanocomposites via a PDC approach. J Am Ceram Soc. 2020;103(2):1385–95.
34. Chen J, Wei X, Zhang J, Luo Y, Chen Y, Wang G, et al. Titanium nitride hollow spheres consisting of tin nanosheets and their controllable carbon-nitrogen active sites as efficient electrocatalyst for oxygen reduction reaction. Ind Eng Chem Res. 2019;58(8):2741–8.

How to cite this article: Awin EW, Günther TE, Loukrakpam R, Schafföner S, Roth C, Motz G. Synthesis and characterization of precursor derived TiN@Si–Al–C–N ceramic nanocomposites for oxygen reduction reaction. Int J Appl Ceram Technol. 2023;20:59–69.
https://doi.org/10.1111/ijac.14234